EFFECTS OF UNIFORM SHEAR ON THE FLOW PAST A CURVED CIRCULAR CYLINDER

José P. Gallardo[*], George K. El Khoury[*], Bjørnar Pettersen[*] and Helge I. Andersson[†]

[*]Norwegian University of Science and Technology, Department of Marine Technology
NO-7491 Trondheim, Norway
e-mail: bjornar.pettersen@ntnu.no

[†]Norwegian University of Science and Technology, Department of Energy and Process Engineering
NO-7491 Trondheim, Norway
e-mail: helge.i.andersson@ntnu.no

Key words: Curved circular cylinder, Shear flow, DNS, Immersed Boundary Method

Abstract. *The effect of uniform shear on the flow past a curved cylinder at a Reynolds number of* 100 *has been studied by means of Direct Numerical Simulations on a staggered Cartesian grid. The non-slip condition at the solid walls was taken into account by a direct forcing Immersed Boundary Method. The geometrical configuration consisted of a quarter-of-ring segment of non-dimensional radius of curvature* 12.5, *and a horizontal extension between the end of the curved segment and the outflow plane. The flow was directed towards the convex face of the quarter-ring, and the non-dimensional shear-rate at the input was set to* $K = 0$ *and* 0.1. *One single shedding frequency prevailed along the entire span of the cylinder for uniform flow* $(K = 0)$ *whereas at a non-dimensional shear-rate of* $K = 0.1$, *the shear flow gave rise to an oblique and cellular vortex shedding pattern with two dominant shedding frequencies decreasing toward the horizontal extension. The dislocations occurred periodically each five shedding cycles and at a local Reynolds number of* 167. *The mean local base pressure for uniform shear gave evidence of a region dominated by a fairly low favourable pressure gradient close to the top of the cylinder which resulted in a longer recirculation bubble in this region than for* $K = 0$.*

1

1 INTRODUCTION

Flows around circular cylinders comprise a variety of complex flow phenomena which depend on the shape and orientation of the cylinder with respect to the flow direction as well as on the incoming flow conditions. The flow past a straight circular cylinder is perhaps the simplest of these configurations, and it is hardly surprising that this flow problem has been extensively investigated during the past decades by means of laboratory experiments and computer simulations. Zdravkovich,[1] for instance, has provided a comprehensive review on this topic.

In many industrial applications, however, the flow past non-uniform circular cylinders is frequently encountered. Such types of configurations give rise to different wake dynamics compared to straight cylinder flows. A ring or torus with a circular cross-section, which is obtained by bending a straight circular cylinder, represents an example of a non-uniform cylinder geometry. Although the flow around a ring has been studied previously,[2–4] most of the studies have been focused on flows with the free stream aligned normal to the plane of curvature of the ring. A variant of the ring-like geometry may be found in offshore structures and marine operations, where hanging risers, anchor lines and pipelines form catenaries whose geometries resemble that of a quarter turn of a ring with a high radius of curvature. Miliou *et al.*[5] used this geometry to investigate the flow past a riser at $Re = 100$ by means of Direct Numerical Simulations (DNS) with the free-stream coming from different directions. In a subsequent work, Miliou *et al.*[6] studied the same geometry with the free stream aligned parallel to the plane of curvature of the cylinder at Reynolds numbers of 100 and 500. In this case, the authors observed different features in the vortex shedding depending on the orientation of the cylinder with respect to the flow direction.

The other parameter affecting the wake in the flow past a circular cylinder, namely the incoming flow condition, is of particular importance to the marine industry since ocean currents interacting with waves, wind and the sea bottom have non-uniform vertical velocity profiles. The experimental[7–10] and numerical[11,12] studies of the flow past a circular cylinder in uniform shear flow have revealed the presence of secondary flows as well as oblique and cellular vortex shedding as a direct consequence of the inflow condition. Due to the shear effect, pressure gradients are generated along the front and rear stagnation lines, causing secondary flows to appear at these locations. The experimental work done by Woo *et al.*[8] estimated magnitudes for the mean velocities induced by these pressure gradients. In addition, the presence of horseshoe vortices may enhance these secondary flows on the rear stagnation line. The numerical simulations of Miliou *et al.*[6] on curved circular cylinder flows predicted the existence of pressure gradients dictated by the geometry along the front and rear stagnation lines. This induced secondary flows along the stagnation lines. It seems therefore interesting to investigate the effects of combining incoming shear flow with a non-uniform geometry like a curved cylinder.

In the present study we perform DNS of the flow past a curved circular cylinder in uniform shear flow. This will enable us to study the effect of a uniform shear-rate on the
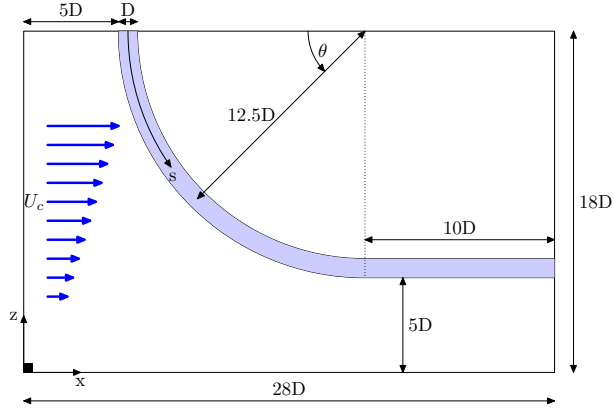
José P. Gallardo, George K. El Khoury, Bjørnar Pettersen and Helge I. Andersson

Figure 1: Computational domain size, geometry and flow configuration shown at the middle (x, z)-plane. The size of the computational domain is $28D$, $11D$ and $18D$ in the x-,y- and z-directions, respectively. The inflow velocity varies linearly in the z-direction, with an average value U_c at the mid height of the computational domain. The spanwise coordinate s is measured along the cross-sectional axis following the curvature of the cylinder from the top plane, varying between 0 and $19.6D$ at the end of the bend.

instantaneous vortex topology, recirculation region as well as on the shedding mechanisms. The previous DNSs with this geometry[5,6] were performed using a spectral/hp element Navier-Stokes solver and a boundary-fitted grid. In the present study the solution of the Navier-Stokes equations is obtained with a Cartesian grid solver, and a direct forcing Immersed Boundary Method (IBM) is used to implement the non-slip boundary condition at the solid surfaces. It is thus intended to check the overall performance of these methods for the complex geometry involved. In order to achieve this comparison, we intentionally considered a convex-shape geometry identical to that studied by Miliou *et al.*[6] with uniform inflow.

2 FORMULATION

2.1 Flow configuration

Figure 1 shows a schematic view of flow past a curved cylinder which is composed of a quarter segment of a ring and a horizontal extension. Of particular importance in curved cylinder flows is the non-dimensional radius of curvature. This dimensionless parameter is defined as the ratio of the radius of curvature of the quarter-ring R to its cross-sectional diameter D. In the present study we consider a flow configuration identical to that of Miliou *et al.*[6] This consists of a quarter-ring with curvature ratio $R/D = 12.5$ and a horizontal extension of length $10D$ between the end of the bend and the outflow plane. Throughout the present paper, the span s is defined as the arc-length of the curved cylinder measured from the top plane; i.e. $s = R\theta$ with θ the angle measured in radians from the top plane.
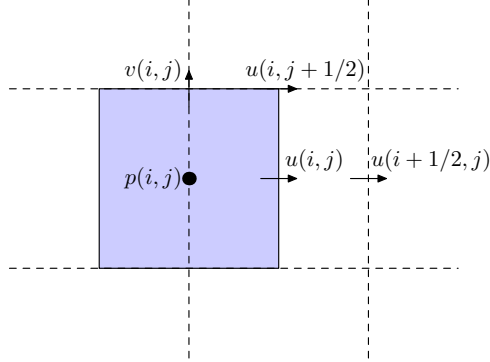
3

Figure 2: Control volumes for the u-velocity (dashed lines) and the pressure (gray) in the staggered grid.

2.2 Governing equations of fluid motion

The dynamics of the flow are described by the time-dependent Navier-Stokes equations for an incompressible Newtonian fluid expressed in non-dimensional form:

$$\frac{\partial u_i}{\partial x_i} = 0, \tag{1}$$

$$\frac{\partial u_i}{\partial t} + u_j \frac{\partial u_i}{\partial x_j} = -\frac{\partial p}{\partial x_i} + \frac{1}{Re} \frac{\partial^2 u_i}{\partial x_j^2}, \tag{2}$$

Here, the Reynolds number is based on the cylinder diameter and the inflow velocity at the mid height of the computational domain, $Re = U_c D/\nu$, with ν the kinematic viscosity. For the simulations presented in this work we set $Re = 100$.

2.3 Numerical method

The governing equations (1) and (2) have been directly solved with the code MGLET. In this finite-volume code, the Navier-Stokes equations for an incompressible fluid are discretised on a staggered Cartesian mesh with non-equidistant grid-spacing.[13,14] The mid-point rule[14] is employed to approximate the fluxes with the variables defined on the control cell shown in figure 2. The velocities $u(i + 1/2, j)$ and $u(i, j + 1/2)$ at the faces of the momentum cell for the u-velocity are obtained by linear interpolation. A central difference scheme is used to approximate the derivatives in the x- and y-directions at the positions $(i + 1/2, j)$ and $(i, j + 1/2)$ respectively, ensuring second order accuracy in the spatial discretization of the convective and diffusive terms.[15]

For the time advancement of the momentum equations an explicit third-order Runge-Kutta scheme is used. The pressure at the new time level $n + 1$ is found by solving the Poisson equation for the pressure correction $\Delta p^{n+1} = p^{n+1} - p^n$ based on the the intermediate velocity fields $\mathbf{u}^*$ computed from the momentum equation (2). The Poisson equation is solved iteratively by the Stones strongly implicit procedure (SIP), producing intermediate pressure p^* and velocity $\mathbf{u}^*$ fields at each iteration. The divergence of the

intermediate velocity fields div($\mathbf{u}^*$) is checked against a defined tolerance ϵ for each iteration. When div(u^*) $\leq \epsilon$ the intermediate pressure and velocity fields are updated at the next time step t^{n+1}.

2.4 Immersed boundary method

At the walls, the non-slip and non-impermeability conditions are taken into account by using a *direct forcing* Immersed Boundary Method (IBM). Basically, the cells at the fluid-solid interface are transformed into internal boundary conditions on the corresponding computational domain by using higher order interpolation from the fluid cells in the vicinity of the body. This method represents a simple way to deal with complex geometries avoiding the need to generate a body fitted grid. A detailed review of the IBM method is found in the work by Mittal and Iaccarino.[16]

The general stencil configuration for the IBM method is depicted in figure 3 for the one-dimensional case. Here ϕ represents one of the velocity components, ϕ_0 is the internal Dirichlet boundary condition, ϕ_r the value at the wall; and ϕ_1, ϕ_2 and ϕ_3 the values in the fluid used for the interpolation. The internal boundary condition based on interpolation from N neighboring cells is determined by the following expression

$$\phi_0 = \left(\sum_{i=1}^{N} \alpha_i \phi_i \right) + \alpha_r \phi_r \tag{3}$$

where α_i and α_r are the interpolation coefficients for the variable ϕ at the fluid cells and the body, respectively.

As mentioned above, MGLET uses a Cartesian staggered grid, which means that the boundaries between velocity and pressure cells do not coincide, as shown in figure 2. The blocking strategy for the IBM method is pressure oriented, then the blocked cells are pressure cells that lie within the surfaces that demarcate the solid walls. According to this criterion, the blocked velocity cells are those touched by the blocked pressure cells.

The interpolation can be either carried out by Lagrange polynomials or using least squares interpolation. It was shown by Peller *et al.*[17] that the interpolation coefficients α_i and α_r depend only on the geometry, thus they can be determined in a preprocessing step. In order to account for three-dimensionality, weighting factors are estimated in the different directions to compute ϕ_0. Finally, the computational representation of the body can be done analytically or using a non-structured mesh consisting of triangles.

2.5 Simulation parameters and implementation

In the present work the dimensions of the grid in each direction are $N_x = 400$, $N_y = 150$ and $N_z = 258$, resulting in a total of 15.48×10^6 grid points. The data for a straight uniform circular cylinder presented by Zdravkovich[1] was used to interpolate the boundary layer thickness δ, obtaining $\delta \approx 0.5D$ at $Re = 100$. In order to adequately resolve the details of the boundary layer and the wake, non-uniform grid spacing is used in

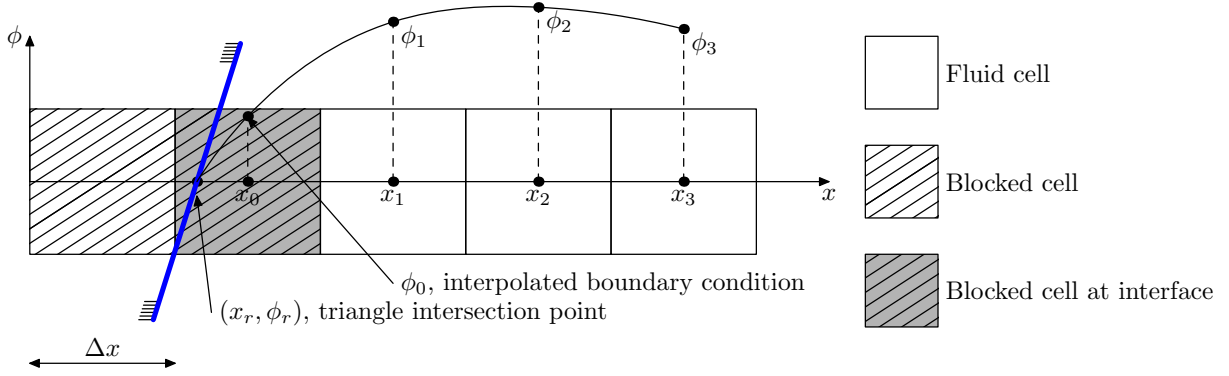Figure 3: One-dimensional stencil for the interpolation in the x-direction using the IBM method; the body boundary corresponds to the thick blue line. Adapted from the work by Peller *et al.*[17]
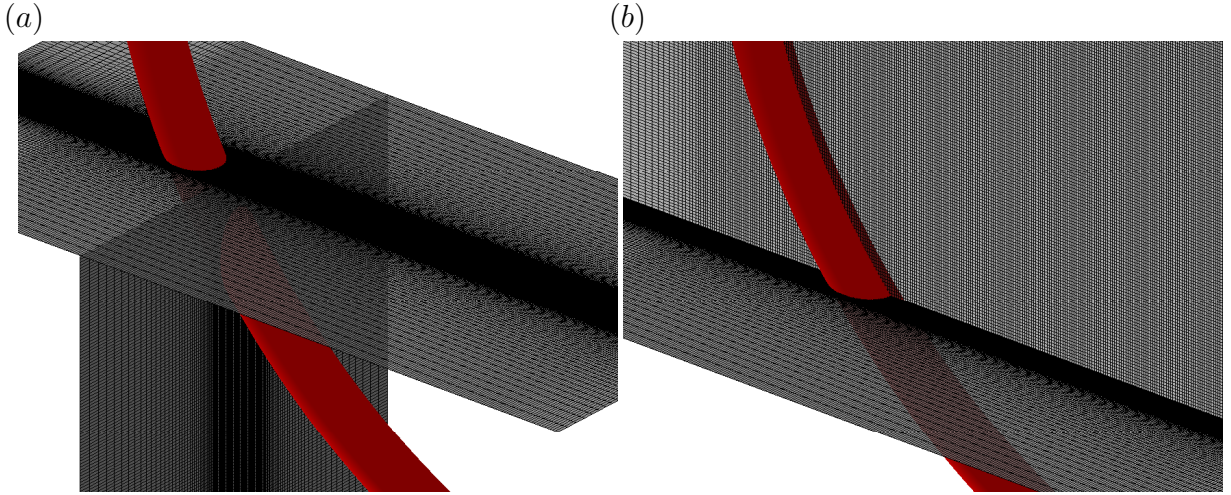

Figure 4: Detail of the $400 \times 150 \times 258$ Cartesian mesh around the curved cylinder . (a) View of the (x, y)- and (y, z)-planes; (b) (x, y)- and (x, z)-planes.

the three spatial directions. The minimum grid spacing for the uniform and shear flow cases are $\Delta x/D = 0.05$, $\Delta y/D = 0.02$ and $\Delta z/D = 0.057$ in the x-, y- and z-directions respectively. Different planes of the mesh close to the body are shown in figure 4, depicting the clustering of points in the vicinity of the body.

Figure 5 shows the blocking of the Cartesian grid by the IBM method in the (x, y)- and (y, z)-planes. The least squares method was chosen as interpolation scheme since it possesses better stability properties than the Lagrange interpolation method.[17] The body composed of a quarter-ring and a horizontal extension were represented by a structured mesh consisting of triangles. The resolution of this mesh was rather high in order to avoid errors in the representation of the curved surfaces. In addition, the following boundary conditions were imposed:

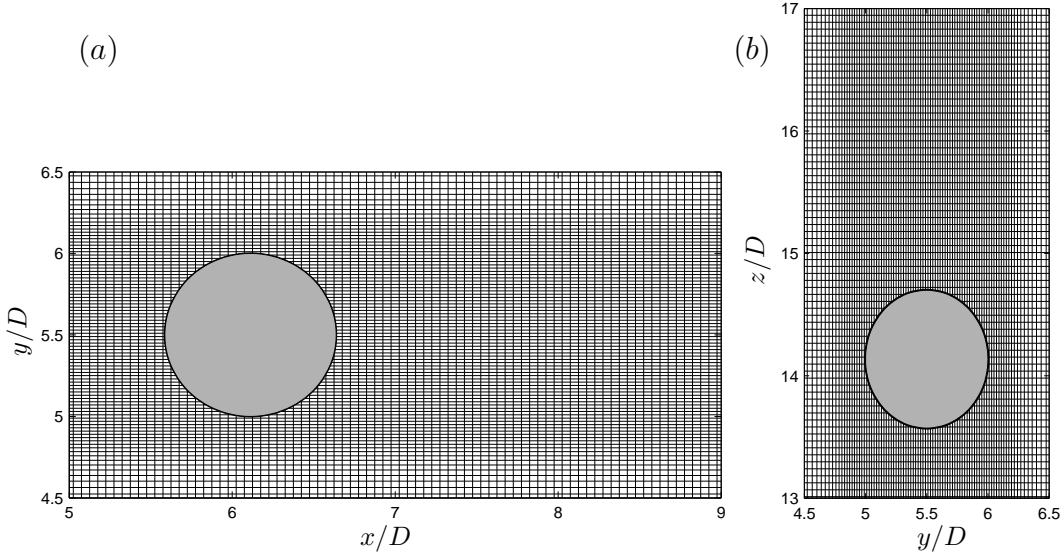1. A free-slip condition on the horizontal top ($z = 18D$) and bottom ($z = 0$) planes as

Figure 5: View of the blocking of cells in the Cartesian mesh by the IBM method. (a) View of the (x, y)-plane at $z/D = 14$; (b) (y, z)-plane at $x/D = 12$.

well as on the vertical sides ($y = 0$ and $11D$) of the computational domain.

2. A uniform shear velocity profile at the inlet,

$$\frac{U_\infty(z)}{U_c} = \frac{Kz}{D} + \frac{U_0}{U_c}, \tag{4}$$

where the non-dimensional inlet shear rate K was set to 0 and 0.1 for the two cases studied. Here, $K = (dU_\infty/dz)D/U_c$, with dU_∞/dz defined as the inflow shear rate; and U_0 is the inflow velocity at the bottom plane ($z = 0$). In this context, we also define the local Reynolds number as $Re_l(z) = U_\infty(z)D/\nu$.

3. At the outlet ($x = 28D$), a Neumann boundary condition was prescribed for the velocities, i.e. $\partial u/\partial x = 0$, $\partial v/\partial x = 0$, and $\partial w/\partial x = 0$; in addition the pressure was set to zero ($p = 0$). This gives a fully developed zero stress condition in order to avoid reflections from the outlet.

The constant time step used for the simulations was $\Delta t = 0.005 D/U_c$ which ensured low values of the maximum Courant number. The flow field evolved to a quasi-periodic state at $tU_c/D \approx 100$, after which statistics were gathered for a period of $300D/U_c$.

The code was run in parallel on an *IBM p575+* machine. A discussion on the efficiency of the parallelization in the code MGLET is found in the work by Manhart *et al.*[13] All the simulations were run on 48 processors, the domain decomposition consisted of 16 processors in the x-direction and 3-processors in the y-direction. In average, the time required to compute one time-step was 2 seconds, resulting in approximately 33 hours to run the 60000 time steps required to gather statistics.

7

3   RESULTS

3.1   Near wake flow

An interesting feature of the flow field is the variation of the mean pressure along the front and rear stagnation lines. This is depicted in figure 6(a) where the non-dimensional mean stagnation pressure $P_s/\rho U_0^2$ is plotted as a function of the span s. Along the front stagnation line, both the uniform ($K = 0$) and shear flow ($K = 0.1$) cases are characterized by a negative pressure gradient ($\partial p/\partial s < 0$) which leads to the development of an axial flow along the convex face of the quarter ring towards the horizontal cylindrical extension. Along the rear stagnation line the uniform flow case ($K = 0$) indicates the presence of a positive gradient along the entire span length ($\partial p/\partial s > 0$). For the shear flow case ($K = 0.1$), however, the mean pressure exhibits a weak negative pressure gradient up to $s/D \approx 4$, where a positive pressure gradient builds-up afterwards.

It is well known that the base pressure distribution (i.e. pressure along the rear stagnation line) influences, among other quantities, the size of the recirculation region which develops in the near-wake due to the separation of boundary layers from the surface of the solid body. This is reflected in figure 6(b) where the non-dimensional local separation length L_s/D is plotted along the span of the quarter-ring segment. Here, L_s is defined as the streamwise distance from the rear stagnation line to where the mean streamwise velocity changes sign from negative to positive. At the top plane, the local separation length for the uniform flow case is approximately $1.5D$; this value remains constant up to $s/D \approx 8$, then it starts decreasing monotonically, reaching zero close to the horizontal part of the cylinder, at $s/D \approx 15$. The variation of L_s for the shear flow case is fairly similar to that of the uniform flow case, but instead of being constant between the spanwise locations 0 and 8 it exhibits a local minimum at $s/D \approx 5$. Such a behaviour, along the first part of the span, has its origin in the pressure coefficient distribution shown in figure 6(a). It is noteworthy that the recirculation length for the shear flow case ($K = 0.1$) is larger than that for the uniform flow case ($K = 0$) at all the spanwise locations.

Further differences between the uniform and shear flow cases are noticeable by looking at the isocontours of mean u- and w-velocities, shown in figures 7(a) to 7(d). When the inflow is uniform ($K = 0$), the lowest mean streamwise velocities in the recirculation region occur close to the top of the cylinder, as seen in figure 7(a), while at a shear rate of 0.1 the region of lowest mean u-velocities is located downwards between $z/D = 12$ and 14 (figure 7c). The contour plot of mean w-velocity for the shear flow case displays a large region with positive vertical velocities on the upper part of the recirculation region (figure 7d); in this case the contours of negative w-velocities are located close to the horizontal extension, with the region of positive velocities above. The uniform flow case, on the other hand, exhibits only a thin region of positive mean w-velocities attached to the rear stagnation line, and negative mean w-velocities prevailing in the rest of the recirculation zone (figure 7b).
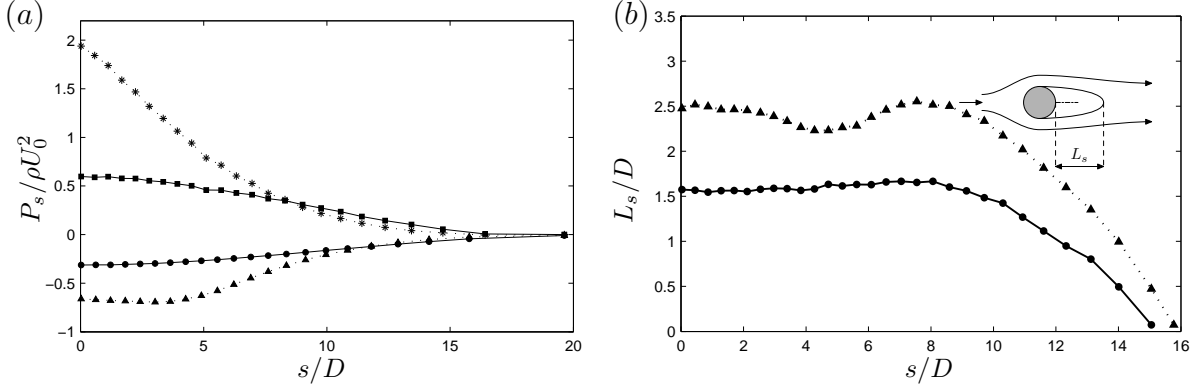
8

Figure 6: Near wake behaviour for the uniform and shear flow cases. (a) Pressure P_s on the front and rear stagnation lines along the span of the curved cylinder. Uniform flow at the inlet ($K = 0$): —■—, stagnation pressure coefficient; —●—, base pressure coefficient. Shear flow at the inlet ($K = 0.1$): $\cdots*\cdots$, stagnation pressure coefficient; $\cdots▲\cdots$, base pressure coefficient. (b) Recirculation length L_s along the span of the curved cylinder: —●— uniform inflow ($K = 0$); —▲— shear inflow ($K = 0.1$).

3.2 Analysis of vortex shedding pattern

In the previous subsection it was discussed how the curved shape and the inflow condition affect the near wake flow. As the flow evolves downstream, the different types of instabilities created close to the body will be amplified, leading to a regular shedding of vortices commonly referred to as a Kármán vortex street. In a similar way as for the near wake flow, the frequency of the shedding and the shape of these vortices will vary according to the geometry and the incoming flow conditions. Figure 8 shows the time evolution of the cross-stream velocity v along a vertical line taken at $x/D = 18$ and the vortical structures depicted by instantaneous λ_2-isosurfaces.[18] The scalar quantity λ_2 defines a region of minimum pressure due to swirling motion in an incompressible fluid based on the second largest eigenvalue of the symmetric tensor $\Omega_{ij}\Omega_{ij} + S_{ij}S_{ij}$, where S_{ij} is the symmetric component of the velocity gradient tensor and Ω_{ij} the antisymmetric part.

$$S_{ij} = \frac{1}{2}\left(\frac{\partial u_i}{\partial x_j} + \frac{\partial u_j}{\partial x_i}\right),\tag{5}$$

$$\Omega_{ij} = \frac{1}{2}\left(\frac{\partial u_i}{\partial x_j} - \frac{\partial u_j}{\partial x_i}\right).\tag{6}$$

The v-velocity signal taken for the uniform flow case ($K = 0$) shown in figure 8(a) is periodic along the vertical line, the pattern clearly corresponds to regular laminar flow, with no distortions occurring; the vortex cores represented as isosurfaces of $\lambda_2 = -0.1$ are vertical close to the body, presenting slight distortions as they move downstream. As previously reported by Miliou et al.,[6] the vortex shedding pattern for $K = 0$ corresponds to that of laminar flow, no dislocations occur despite the non-uniform geometry of the cylinder. A question that remains open here is whether cellular vortex shedding will occur or not if the radius of curvature R is increased; this topic is currently under investiga-
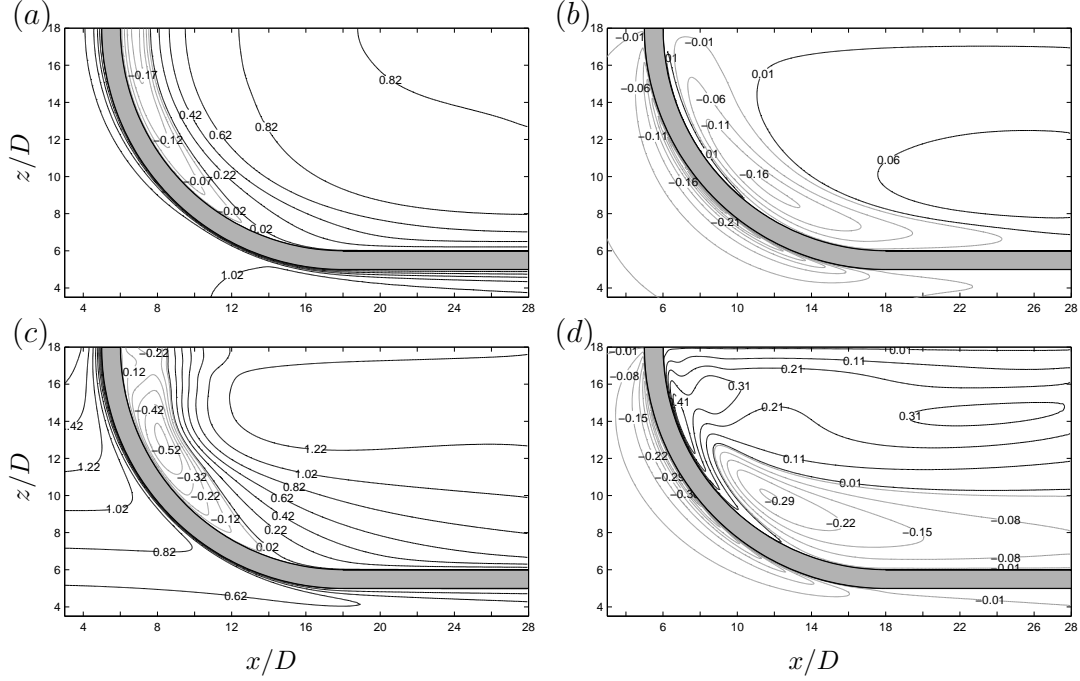
Figure 7: Isocountours of mean streamwise and vertical velocities in the (x, z)-plane. (a) Mean u-velocities for the uniform flow case; (b) mean w-velocities for the uniform flow case; (c) mean u-velocities for the shear flow case; and (d) mean w-velocities for the shear flow case.

tion. For the shear flow case ($K = 0.1$), on the other hand, periodic dislocations can be identified in the upper part of the domain in the time evolution of v, as seen in figure 8(b). These dislocations arise at a local Reynolds number of 167 ($z/D = 15.7$), close to the Reynolds number range at which the mode A instabilities described by Williamson[19] appear. Furthermore, the vortex cores represented as isosurfaces of $\lambda_2 = -0.1$ display a high degree of obliqueness relative to the vertical, also a consequence of the shear rate imposed.

The plot of the time traces of the cross-stream velocities at $x/D = 18$ and at six different positions along the z-axis shown in figure 9(a) gives a clear picture of the periodic behaviour of the uniform flow case. With the exception of the time trace at $z/D = 8$, where the vortex shedding is less energetic, all the traces plotted have almost the same amplitude. In this case the suppression of the vortex shedding occurs at $z/D \approx 7$. At an inflow shear rate of 0.1, the trace signals of the v-velocities clearly differ from those corresponding to uniform inflow. The behaviour in this case is quasi-periodic, with the suppression of vortex shedding occurring around $z/D \approx 10$. The periodic dislocations shown in figure 8(b) are due to the splitting of the Kármán vortices as they are shed from the upper segment of the curved cylinder. This splitting, for instance, can be identified in the v-velocity trace at $z/D = 16$; here the signal exhibits a low frequency modulation and the dislocations occur each five shedding cycles.
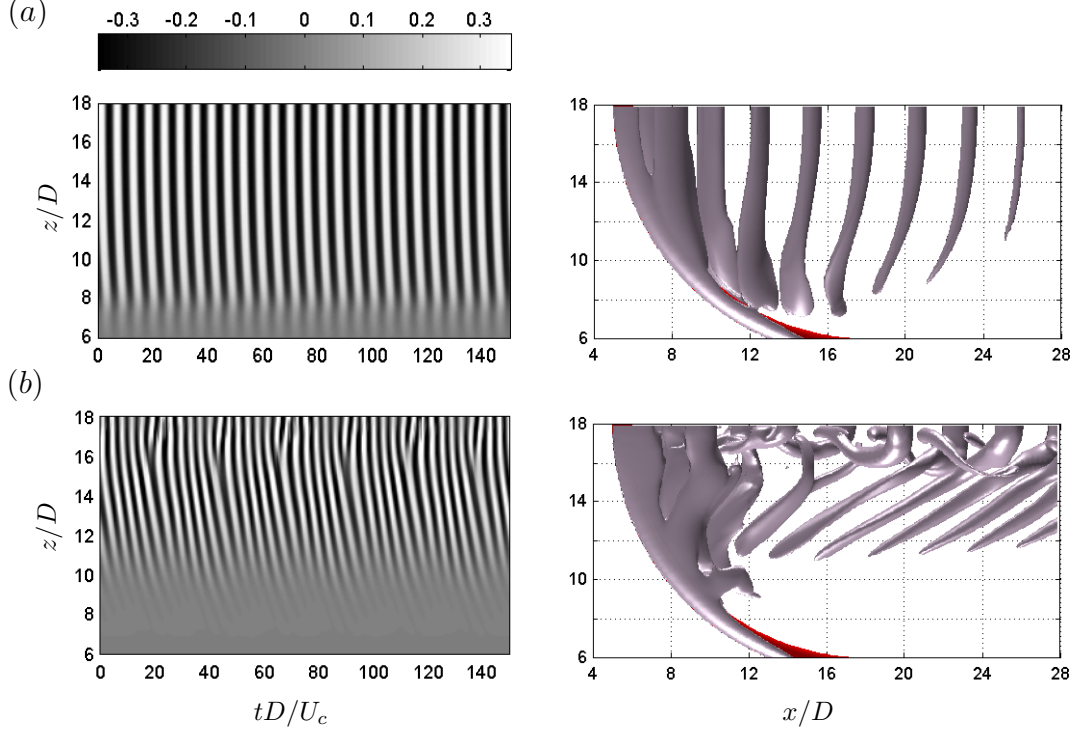
10

Figure 8: Time evolution of cross-stream velocity v along a sampling line taken at $x/D = 18$ in the middle (x, z)-plane $(y/D = 5.5)$ to the left, and vortex cores represented as isosurfaces of $\lambda_2 = -0.1$ to the right. (a) Uniform inflow; (b) shear inflow.

In order to identify the dominant shedding frequencies, a spectral analysis with basis on the time-domain signals of the v-velocity has been carried out. The sampling rate of the signals is $100U_c/D$, which is lower than the maximum value $1/\Delta t = 200U_c/D$ required to avoid aliasing effects (see Persillon & Braza[20]). The dominant shedding frequency obtained by Fourier analysis for the uniform flow case is $fD/U_c = 0.176$, prevailing along the whole sampling line, with no cellular arrangement of the vortices. This is in good agreement with the frequency 0.1761 reported by Miliou et al.[6] for their convex configuration. It has been shown in previous studies of circular cylinders that when uniform shear flow is imposed as an inflow boundary condition, the vortex shedding will arrange in a cellular pattern; see for instance the work by Mukhopadhyay et al.[11] This is the case in figure 10(a), where the dominant frequencies are plotted versus the local Reynolds numbers. The St-Re curve exhibits two frequency cells at $fD/U_c = 0.240$ and 0.283, with lengths $5.63D$ and $2.37D$ respectively; here the dislocation occurs at $Re_l = 167$ $(z/D = 15.7)$. Shown in figure 10(b) are the isocountours of streamwise vorticity ω_x in the middle (x, z)-plane, displaying the highest intensities close to the top of the computational domain. Close to the upper part of the body, regions of streamwise
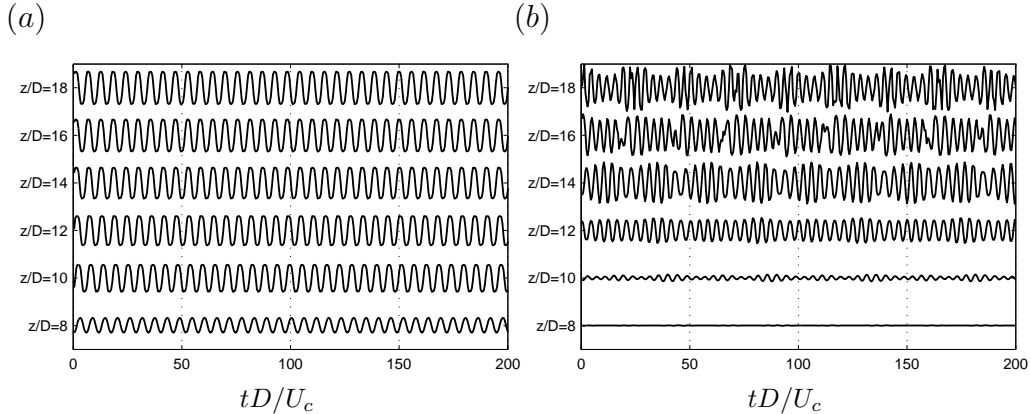
11

(a)　　　　　　　　　　　　　　　(b)

Figure 9: Time traces of cross-stream velocity v along a sampling line taken at $x/D = 18$ in the middle (x, z)-plane $(y/D = 5.5)$. (a) Uniform inflow; (b) shear inflow.

vorticity with opposite sign can be identified, triggering the splitting of the main oblique vortices (Kármán vortices). This fragmentation was observed by Persillon & Braza[20] in their numerical simulations for a straight cylinder when they increased the Reynolds number beyond 190.

Further insight in the vortex shedding behaviour can be gained from the isosurfaces of instantaneous streamwise and vertical vorticity, which have been plotted in figure 11. The white isosurfaces correspond to the primary vortex cores represented by ω_z, while the black isosurfaces depict the streamwise vorticity ω_x. The shape of the primary vortex cores shown in figure 11(a) is similar to those expected for a straight circular cylinder (i.e. vertical). Furthermore, this particular geometry triggers streamwise vorticity in the lower part of the domain, affecting the vortex shedding pattern with respect to that of a straight circular cylinder. The streamwise vorticity for the shear flow case exhibits two distinct behaviours related to the presence of uniform shear at the inlet. Close to the top of the computational domain, where the highest local velocities of the free-stream occur, the presence of streamwise vorticity reveals the instabilities that lead to the splitting of the primary vortices discussed previously. Below this region, the isosurfaces of streamwise vorticity are strongly slanted and are clearly related to the oblique shedding of vortices. The cellular pattern of the vortex shedding and the obliqueness of the vortices behind a bluff body has been previously reported.[7–12] Most of these studies, however, consider a straight cylindrical geometry. Hence, further studies with different shear rates are relevant to better understand the interaction of the shear flow with this geometry. From figure 11(a), for instance, it was shown that streamwise vorticity arises as an effect of the curved geometry for the uniform flow case; the tilting of the vorticity induced by different shear rates may have either an adverse or favourable effect when interacting with the vorticity induced by geometry effects.

Finally, in order to study the evolution of the wake for the shear flow case, the instantaneous streamwise vorticities ω_x and ω_z were plotted in three consecutive planes in figure
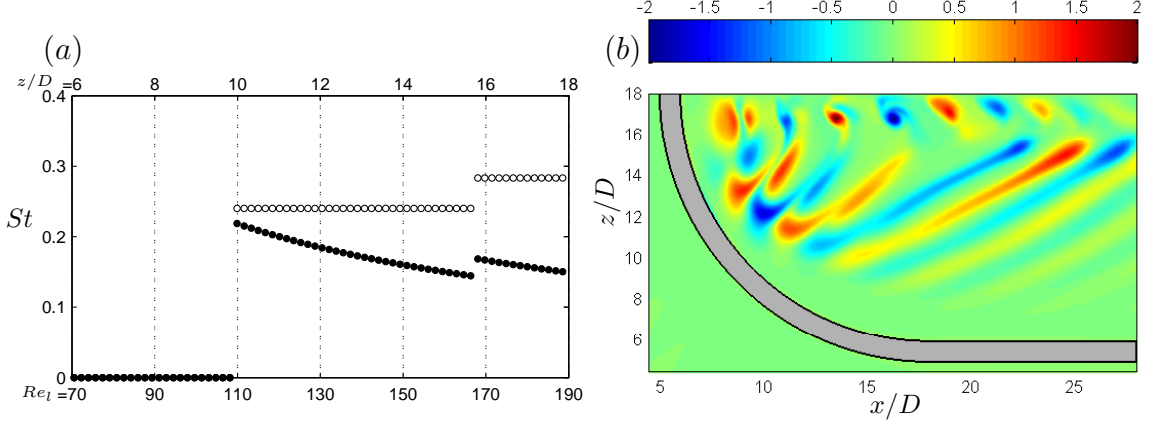
12

Figure 10: (a) Strouhal frequencies along a sampling line taken at $x/D = 18$ in the middle (x, z)-plane $(y/D = 5.5)$. Shear flow case, $\bullet$, St based in the local inflow velocity $U_\infty(z)$; $\circ$, St based in U_c. (b) Isocontours of instantaneous streamwise vorticity ω_x in the middle (x, z)-plane $(y/D = 5.5)$.

12. The instantaneous streamwise vorticities in the (y, z)-planes shown in figure 12(a) give a clear picture of the evolution of ω_x in the x-direction. The plane at $x/D = 7$ is located within the recirculation region in the upper portion of the cylinder, here we observe two parallel layers of ω_x with opposite sign corresponding to the bended vortex filaments of ω_y induced by the shear rate.[8] The plane at $x/D = 12$ exhibits a similar pattern at the lower part of the curved cylinder, but the layers of ω_x here have different sign than those at $x/D = 7$; on the upper half of this plane negative values of ω_x prevail. At $x/D = 18$ the streamwise vorticity is split into several regions of counter rotating vorticity. In a similar way, figure 12(b) depicts the pattern for the vertical vorticity ω_z on three consecutive (x, y)-planes. Since the vortex shedding starts above $z/D = 10$, only two regions of ω_z appear at $z/D = 8$, here the flow could be regarded as locally stationary. At $z/D = 12.5$, where the local Reynolds number is 135, a clear pattern of vortex shedding is represented by the isocontours of ω_z. Close to the top of the domain at $z/D = 17.5$ the pattern of ω_z is more irregular than that at $z/D = 12.5$, the ω_z-cores are spread, covering a larger area at this vertical location; here $Re_l = 185$, i.e. within the range at which the mode A instability occurs,[19] thus the wake instabilities will be amplified as they are transported downstream.

4 CONCLUSIONS

In this work, DNS of the flow past a curved circular cylinder at $Re = 100$ is performed to study the influence of the curvature and different inflow conditions on the wake dynamics. In order to compare our results with the study by Miliou $et\ al.$,[6] a uniform inflow profile was considered as inflow boundary condition in an initial stage. Subsequently, the inflow
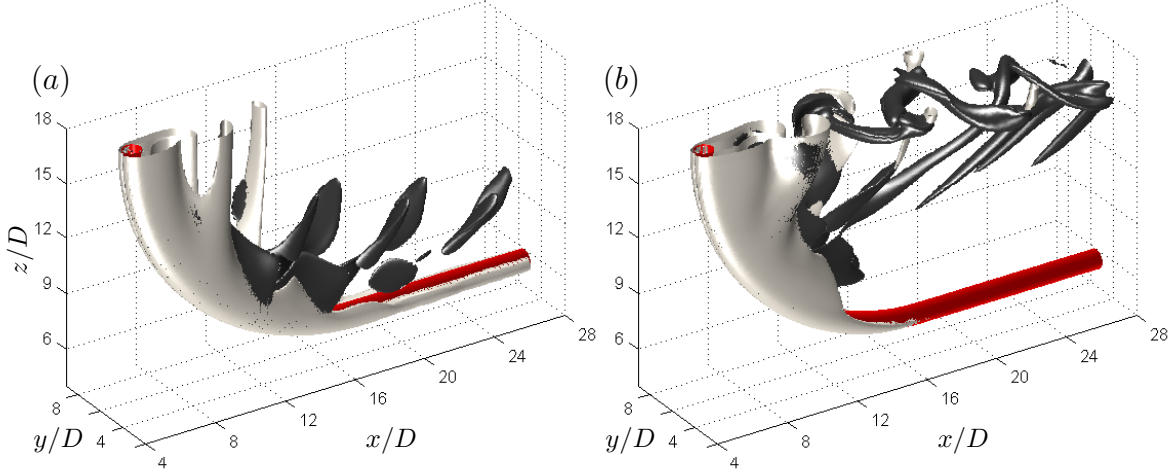
Figure 11: Detail of isosurfaces of instantaneous vorticity ω_x (black) and ω_z (white). (a) Uniform flow, isosurfaces of $\omega_x = \pm 0.3$ and $\omega_z = \pm 1.2$; (b) shear flow, isosurfaces of $\omega_x = \pm 0.7$ and $\omega_z = \pm 1.6$.

condition was changed to uniform shear with a shear rate of $K = 0.1$.

In general terms, good agreement was obtained between the present work and the results reported by Miliou *et al.*[6] for the uniform flow case. As a qualitative comparison, the vortical structures depicted in figure 8 exhibited the same shape as those reported in the mentioned study. Initially the vortex cores are vertical, then, as they travel further downstream, small distortions appear in the λ_2-isosurfaces. Additionally, the Strouhal frequency obtained for the uniform case ($fD/U_c = 0.176$) was the same as that reported by Miliou *et al.*[6]

Concerning the recirculation region, the base pressure gradient for the uniform flow case was adverse along the whole span, while the shear flow case exhibited a region of weak favourable pressure gradient. This clearly affected the distribution of velocities in the recirculation zone and the size of the recirculation bubble, which was larger than the recirculation bubble for the uniform flow case along the whole span, despite the local minimum observed in figure 6(b). Further downstream in the wake, the time analysis for the shear flow case revealed two distinct cells of different shedding frequency with values $fD/U_c = 0.240$ and 0.283. The computed length of these cells was $5.63D$ and $2.37D$, with a dislocation occurring at $z = 15.7D$. Furthermore, it was estimated that the dislocations occurred periodically each five shedding cycles. The analysis of vortical flow structures based on the instantaneous λ_2- and vorticity-isosurfaces revealed streamwise vorticity induced by the geometry for the uniform flow case, and streamwise wake instabilities for the shear flow case. Additionally, the shear flow case was characterized by oblique vortex shedding as the wake evolved downstream.

The performance of the IBM method was very promising when performing the simulations using this curved cylinder geometry embedded in a Cartesian mesh. It is therefore
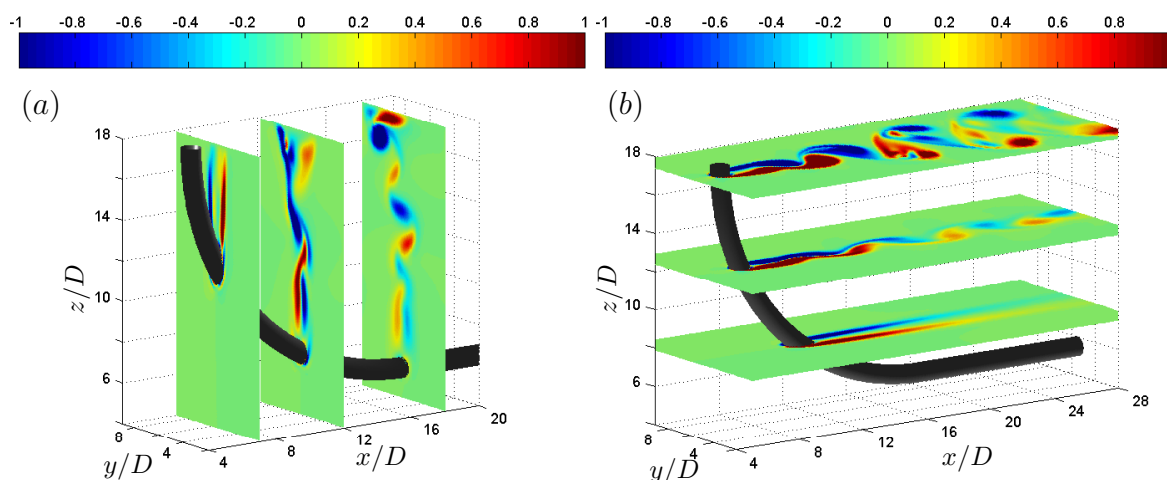
14

Figure 12: Instantaneous isocontours of vorticity for the shear flow case. (a) ω_x in the (y,z)-planes at $x/D = 7$, 12 and 18; (b) ω_z in the (x,y)-planes at $z/D = 8$, 12.5 and 17.5.

intended to extend this study to other shear rates and radii of curvature, contributing thus to the knowledge of the flow physics of the wake past such geometries.

ACKNOWLEDGMENTS

REFERENCES

[1] M. M. Zdravkovich, *Flow Around Circular Cylinders, Vol. 1 Fundamentals*, Oxford University Press, (1997).

[2] T. Leweke and M. Provansal, The flow behind rings: bluff body wakes without end effects, *J. Fluid Mech.*, **288**, 265–310 (1995).

[3] D. R. Monson, The effect of transverse curvature on the drag and vortex shedding of elongated bluff bodies at low Reynolds number, *J. Fluids Eng.*, **105**, 308–318 (1983).

[4] M. Takamoto and K. Izumi, Experimental observation of stable arrangement of vortex rings, *Phys. Fluids*, **24**, 1582–1583 (1981).

[5] A. Miliou, S. J. Sherwin and J. M. R. Graham, Fluid dynamic loading on curved riser pipes, *J. Offshore Mech. Arct.*, **125**, 176–182 (2003).

[6] A. Miliou, A. De Vecchi, S. J. Sherwin and J. M. R. Graham, Wake dynamics of external flow past a curved circular cylinder with the free stream aligned with the plane of curvature, *J. Fluid Mech.*, **592**, 89–115 (2007).

15

[7] W. A. Mair and P. K. Stansby, Vortex wakes of bluff cylinders in shear flow, *SIAM J. Appl. Math.*, **28**, 519–540 (1975).

[8] C. H. G. Woo, J. E. Cermak and J. A. Peterka, Secondary flows and vortex formation around a circular cylinder in constant-shear flow, *J. Fluid Mech.*, **204**, 523–542 (1989).

[9] D. Sumner and O. O. Akosile, On uniform planar shear flow around a circular cylinder at subcritical Reynolds number, *J. Fluids Struct.*, **18**, 441–454 (2003).

[10] M. Kappler, W. Rodi, S. Szepessy and O. Badran, Experiments on the flow past long circular cylinders in a shear flow, *Exp. Fluids*, **38**, 269–284 (2005).

[11] A. Mukhopadhyay, P. Venugopal and S. P. Vanka, Oblique vortex shedding from a circular cylinder in linear shear flow, *Comput. Fluids*, **31**, 1–24 (2002).

[12] J. H. Silvestrini and E. Lamballais, Direct numerical simulation of oblique vortex shedding from a cylinder in shear flow, *Int. J. Heat Fluid Flow*, **25**, 461–470 (2004).

[13] M. Manhart, F. Tremblay and R. Friedrich, MGLET: A parallel code for efficient DNS and LES of complex geometries, In *Parallel Computational Fluid Dynamics 2000*, Elsevier Science B.V., 449–456, (2001).

[14] M. Manhart , A zonal grid algorithm for DNS of turbulent boundary layers, *Comput. Fluids*, **33**, 435–461 (2004).

[15] J. H. Ferziger and M. Perić, Computational Methods for Fluid Dynamics, 3th Edition, *Springer: Berlin*, (2002).

[16] R. Mittal and G. Iaccarino, Immersed boundary methods, *Annu. Rev. Fluid Mech.*, **37**, 239–261 (2005).

[17] N. Peller, A. Le Duc, F. Tremblay and M. Manhart, High-order stable interpolations for immersed boundary methods, *Int. J. Numer. Meth. Fluids*, **52**, 1175–1193 (2006).

[18] J. Jeong and F. Hussain, On the identification of a vortex, *J. Fluid Mech.*, **285**, 69–94 (1995).

[19] C. H. K. Williamson, The existence of two stages in the transition to three-dimensionality of a cylinder wake, *Phys. Fluids*, **31**, 3165–3168 (1988).

[20] H. Persillon and M. Braza, Physical analysis of the transition to turbulence in the wake of a circular cylinder by three-dimensional Navier Stokes simulation, *J. Fluid Mech.*, **365**, 23–88 (1998).